Research Article

Ebrahem A. Algehyne, Fahad Maqbul Alamrani, M. M. Seada, Anwar Saeed*, and Gabriella Bognár*

Numerical examination of the chemically reactive MHD flow of hybrid nanofluids over a two-dimensional stretching surface with the Cattaneo–Christov model and slip conditions

https://doi.org/10.1515/phys-2025-0140
received December 02, 2024; accepted February 21, 2025

Abstract: Energy deficiency is one of the most challenging issues of the present world due to its increasing demand in industrial and technological processes. To address this issue, energy efficiency improvement is essential. Hybrid nanofluids have significant applications in the industrial and engineering sectors because of their higher thermal conductivity compared to conventional nanofluids. Keeping these important applications in mind, this work investigates the two-dimensional magnetohydrodynamic hybrid nanofluid flow on shrinking/stretching sheets under the impact of the Cattaneo–Christov model, suction/injection, thermal radiation, and slip effects. The hybrid nanofluid is formed by mixing nanoparticles of copper and alumina with a base fluid. The main equations are converted to a dimensionless form using appropriate variables. The model is evaluated by using the bvp4c built-in code in MATLAB. As main outcomes of the work, it is revealed that the increasing magnetic parameter enhances the skin friction of hybrid nanofluids; however, a reverse influence is noticed in the velocity curve. An upsurge in thermal radiation and Eckert number causes a substantial augmentation in the heat transfer rate, and a similar influence is observed in the temperature profile. The mass transfer rate shows a decreasing behavior through growth in chemical reactions and the Schmidt number. This investigation offers comprehensive insights into optimizing heat transfer and fluid flow in various engineering and industrial applications, such as thermal management, manufacturing processes, chemical reactors, and microfluidic devices.

Keywords: MHD, Cattaneo–Christov model, suction/injection, stretching/shrinking sheet

*** Corresponding author: Anwar Saeed,** Department of Mathematics, Abdul Wali Khan University, Mardan 23200, Khyber Pakhtunkhwa, Pakistan, e-mail: anwarsaeed769@gmail.com
*** Corresponding author: Gabriella Bognár,** Institute of Machine and Product Design, University of Miskolc, Miskolc-Egyetemváros, 3515, Hungary, e-mail: gabriella.v.bognar@uni-miskolc.hu
Ebrahem A. Algehyne: Department of Mathematics, Faculty of Science, University of Tabuk, P.O. Box 741, Tabuk, 71491, Saudi Arabia; Nanotechnology Research Unit (NRU), University of Tabuk, Tabuk, 71491, Saudi Arabia
Fahad Maqbul Alamrani: Department of Mathematics, Faculty of Science, University of Tabuk, P.O. Box 741, Tabuk, 71491, Saudi Arabia
M. M. Seada: Department of Physics, College of Science and Humanities, Prince Sattam bin Abdulaziz University, Al-Kharj, 16273, Saudi Arabia; Physics Department, Faculty of Science, Tanta University, Tanta, 31527, Egypt

Nomenclature

x, y	Cartesian coordinates
u, v	components of velocity
B_0	strength of the magnetic field
T	temperature
T_w	temperature of the sheet
C_w	concentration on the wall
C	concentration
Sc	Schmidt number
Pr	Prandtl number
Rd	radiation factor
Kr	chemical reactivity parameter
α	velocity slip parameter
s	suction/injection factor
Ec	Eckert number
γ	thermal slip parameter
λ	stretching and shrinking surface
λ_1	thermal relaxation time of heat diffusion
λ_2	concentration relaxation time of mass diffusion
δ	Deborah number due to relaxation time of heat diffusion
β	Deborah number due to relaxation time of mass diffusion
χ	concentration slip parameter

D_B	coefficient of Brownian diffusivity
$\sqrt{\mathrm{Re}_x}\, C_{fx}$	coefficient of skin friction
$\frac{\mathrm{Sh}_x}{\sqrt{\mathrm{Re}_x}}$	Sherwood number
q_r	radiative heat fluidity
$\frac{\mathrm{Nu}_x}{\sqrt{\mathrm{Re}_x}}$	Nusselt number
M	magnetic factor
v_0	suction velocity
Re_x	Reynold number
A	spatial slip constant

1 Introduction

Magnetohydrodynamics (MHD) studies the performance of electrically conducting fluids, like saltwater and plasma, using magnetic field effects. In this phenomenon, the interaction between the motion of fluids and the magnetic field induces electrical currents, which in turn generates additional magnetic fields. These interactions can significantly alter the fluid flow patterns, leading to phenomena such as magnetic drag reduction, flow stabilization, and generation of complex flow structures. MHD fluid flow can significantly influence the analysis of thermal flow in heat transfer processes [1]. The occurrence of magnetic fields can modify the thermal conductance and thermal capability of fluids, causing variations in the thermal distribution within the system [2]. Additionally, MHD effects can influence convective heat transfer, affecting the heat exchange process efficiency in diverse engineering applications like nuclear reactors, metallurgical processes, and geophysical phenomena like the Earth's magnetosphere [3,4]. Electrically conducted fluid flow is therefore essential for adjusting heat transfer systems, enhancing their performance, and confirming the protection and reliability of technological uses. Thermal analysis or MHD dual diffusive Jeffery fluid flow in holes of discs and ducts was performed by Khan *et al.* [5] under effects of various rotations. These authors have observed that the transverse velocity of fluids is retarded with the increase in magnetic and Maxwell factors in all the four scenarios. Mahabaleshwar *et al.* [6] inspected the effects of MHD on CNT flow and thermal flow on a surface under thermally radiative impacts and a thermal sink/source. MHD fluid flow has diverse applications across multiple domains. In power generation, MHD generators harness the interaction between a conducting fluid and the magnetic field to efficiently convert kinetic energy into electricity, particularly in conjunction with nuclear reactors [7]. Space exploration benefits from MHD thrusters that use plasma and magnetic fields for propulsion in the vacuum of space [8]. Additionally, MHD pumps and compressors find applications in aerospace, energy production, and chemical processing for precise fluid transport and compression [9]. In nuclear fusion research, MHD effects are vital for designing magnetic confinement devices like tokamaks, advancing the quest for clean and sustainable energy sources. These applications highlight the broad impact and versatility of MHD fluid flow across scientific, industrial, and technological realms.

The study of fluid flow over stretching and shrinking sheets describes the behavior of viscous fluids on a surface that either expands or contracts continuously [10]. This phenomenon is commonly seen in many engineering applications like polymer processing, coating, and fiber spinning [11]. On a stretching sheet, the fluid tends to stretch along the sheet, resulting in a rise in velocity and a thermal layer on the surface of the sheet [12]. Conversely, on a shrinking sheet, the fluid normally squeezes, resulting in decreased velocity and a thicker boundary layer [13]. These flow patterns significantly affect the velocity and thermal plots near the sheet, influencing the thermal flow. Fluid flow over a contracting or expanding sheet significantly affects heat transfer processes by altering the boundary layer characteristics and velocity profiles [14]. On a stretching sheet, the fluid adjacent to the surface experiences increased stretching, leading to a reduction in the size of the layer at the frontier and an enhancement in velocity gradients [15]. This intensified velocity promotes heat transfer from the sheet to fluid, resulting in augmented convective heat transfer rates. Such phenomena find applications in industrial processes like polymer production, where controlling cooling rates is significant for product quality [16]. Conversely, on a shrinking sheet, the fluid is compressed, leading to an increase in layer thickness near the edge and a reduction in velocity gradients [17]. This decreased velocity hampers convective heat transfer rates, impacting processes such as film cooling in gas turbines or heat dissipation in electronics. Additionally, the alterations in flow characteristics on both stretching and shrinking sheets influence the development of a thermal layer at the boundary and formation of thermal patterns, affecting temperature distributions and thermal gradients along the surface [18]. Kumar *et al.* [19] studied the thermal transportation and flow phenomenon for nanofluid flow on an extending and a shrinking sheet with porous behavior. Khan *et al.* [20] scrutinized the fluid movement on a contracting and an extending sheet with heterogeneous as well as homogeneous chemical reactivity effects.

The movement of fluid on a surface with effects of suction or injection involves the manipulation of fluid dynamics to alter the surface properties. Suction involves

the removal of fluid from the surface, which can alter the layer thickness near the edge and affect drag forces [21]. This can affect the overall flow pattern and velocity distribution near the surface. On the other hand, injection introduces fluid onto the surface, potentially changing surface conditions and creating additional shear stresses. These impacts influence various features of the flow, including adhesion, friction, and heat transmission characteristics. In practical applications, such as drag reduction in aerodynamics or control of cooling processes, controlling the suction or injection effects is essential for optimizing the performance and achieving desired outcomes. The mass transfer phenomenon under Soret and Dufour effects in viscous Casson nanofluid flow over an extending surface was discussed by Ilango and Lakshminarayana [22]. Yasmin [23] studied the heat and mass transfer phenomena of hybrid nanofluids past a stretching surface with impacts of thermal radiation and gyrotactic microorganisms. Mehmood *et al.* [24] examined the influences of suction as well as injection on nanofluids flowing on a vertically stretched surface subject to radiative and bio-convective effects. The effect of Brownian motion and thermophoresis on MHD Casson nanofluid flow past a stretching surface was studied by Ilango and Lakshminarayana [25]. Mahesh *et al.* [26] deliberated on CNTs' impacts on a radiative Marangoni MHD fluid flow with injection and suction effects. Song *et al.* [27] investigated impacts of suction injection on fluid flow through the space between two surfaces. Fluid movement on a surface with injection/suction has significant impacts on the heat transfer process [28]. Nihaal and Mahabaleshwar [29] considered the Buongiorno model to investigate the heat and mass transfer of hybrid nanofluid flow over a cylinder embedded in a porous medium. MS and Pallavarapu [30] examined Joule heating and slip effects to discuss the entropy analysis of Casson nanofluid flow over a stretching surface. Suction modifies the size of the layer at the boundary near the surface, effectively decreasing the thermal resistance between the fluid and the solid. This reduction in the size of the layer at the boundary enhanced convective heat transfer by significantly promoting the turbulent and fluid velocity close to the surface. As a result, heat is more efficiently transported away from the surface, leading to improved cooling performance in various engineering applications. Conversely, the injection of fluid onto the surface alters the thermal layer boundary, affecting temperature gradients and convective heat transfer coefficients. Depending on the specific conditions, injection may either enhance or impede heat transfer. For instance, injecting a cooler fluid can effectively lower the surface temperature, while injecting a warmer fluid can elevate it. Moreover, an injection can induce localized heating or cooling effects depending on the fluid's properties and the injection rate. These changes in convective heat transfer due to suction or injection have wide-ranging applications in cooling devices, heat exchangers, and thermal management systems. Gopi Krishna *et al.* [31] studied the radiative Jeffery fluid flow on a surface with impressions of suction and injection. Many such studies can be observed in the studies of Reddy *et al.*, Bachok *et al.*, Asibor *et al.*, Aly *et al.*, and Asibor *et al.* [32–36].

The Cattaneo–Christov model represents a significant advancement in understanding mass and heat flux phenomena, particularly in the flow of fluid. This theory builds upon classical theories such as Fourier's [37] heat diffusion and Fick's [38] mass diffusion by integrating the influences of thermal relaxation stresses and convective derivatives. Mahariq *et al.* [39] considered the ternary hybrid nanofluid flow on a flat plate solar collector through the Brinkman model to examine heat and mass transfer phenomena. The Cattaneo theory [40] initially introduced modifications to Fourier's model, considering the additional thermal relaxation stresses that arise due to the finite speed of heat propagation. Christov [41] further extended this model by changing PDEs with the Oldroyd upper convective derivative, accounting for non-local effects and improving the accuracy of predictions. The inclusion of these modifications enhances the model's ability to describe heat and mass transfer phenomena in situations where traditional theories fall short, such as high-speed flows or systems with non-negligible relaxation times [42]. The combined analysis of heat and mass transfer holds significant importance in various engineering applications, such as energy generation, nuclear reactor cooling, electronics cooling, tissue heat conduction, frost protection in agriculture, air conditioning, desalination, and food processing [43,44]. By capturing the coupling between thermal and concentration fields more accurately, the Cattaneo–Christov model gives an insightful understanding of heat and mass transfer procedures in various practical applications. For instance, in fluid flow over surfaces, the model can elucidate how thermal relaxation affects the temperature gradients and convective heat transfer rates, influencing heat dissipation and thermal management in engineering systems. Additionally, it can help optimize processes like cooling in electronic devices, thermal insulation design, and heat exchanger performance, ultimately leading to more efficient and reliable engineering designs. Overall, the Cattaneo–Christov model [45] represents an important tool for advancing the understanding of heat and mass transfer phenomena and their impacts on fluid flow over surfaces, with broad implications for diverse industrial and scientific fields. Reddy *et al.* [46] considered the Cattaneo–Christov model to investigate the

entropy generation of MHD Williamson nanofluid through a stretching surface. Ullah *et al.* [47] investigated on the mass and heat transfer of Jeffery fluid flow on a sheet with behavior of Cattaneo–Christov heat and mass flux phenomena. The effect of chemical reaction and heat source on non-Newtonian hybrid nanofluid over a porous stretching sheet was studied by Vindokumar Reddy *et al.* [48].

In a close investigation of the aforementioned studies, various scientists operated on different flow models to examine the behavior of thermophysical constraints of viscous fluid, nanofluid, and hybrid nanofluid assuming various nanoparticles across a shrinking/stretching surface. This work discovers the importance of slips and suction/injection on the flow of hybrid nanofluid comprising the nanoparticles of alumina and copper across a shrinking/stretching surface with a fixed magnetic field. The model considers heat and mass flow phenomena of a hybrid nanofluid with the impacts of the Cattaneo–Christov model, Joule heating, viscous dissipation, velocity, thermal, and concentration slips. The bvp4c code is used in MATLAB software to obtain the numerical and graphical solutions of the proposed model. Additionally, the results of this work were compared with previous literature, confirming the accuracy and validity of our findings.

2 Mathematical structure

Consider the MHD viscous hybrid nanofluid flow over a sheet that is both stretching and shrinking. The Cattaneo–Christov model, suction/injection, slips, and thermal radiation impacts are considered in this study. The flow is induced with a constant magnetic field in the direction normal to the flow field. We suppose that $u_w(x) = ax$ is the velocity of sheet that is either shrinking or stretching, as shown in Figure 1(a) and (b). Furthermore, $v_0 = -\sqrt{av_f}\, s$ is the constant mass flux velocity. The convective constraints at the boundary are considered in the model. We also assume that T_w and C_w are the surface temperature and concentration, respectively. T_∞ and C_∞ are the free-stream temperature and concentration, respectively. The continuity, temperature, and concentration equations for the flow problem are described in the studies of Waini *et al.* and Shehzad *et al.* [49,50]:

$$\frac{\partial u}{\partial x} + \frac{\partial u}{\partial y} = 0, \tag{1}$$

$$u\frac{\partial u}{\partial x} + v\frac{\partial u}{\partial y} = \left(\frac{\mu_{\text{hnf}}}{\rho_{\text{hnf}}}\right)\frac{\partial^2 u}{\partial y^2} - \left(\frac{\sigma_{\text{hnf}}}{\rho_{\text{hnf}}}\right)B_0^2 u, \tag{2}$$

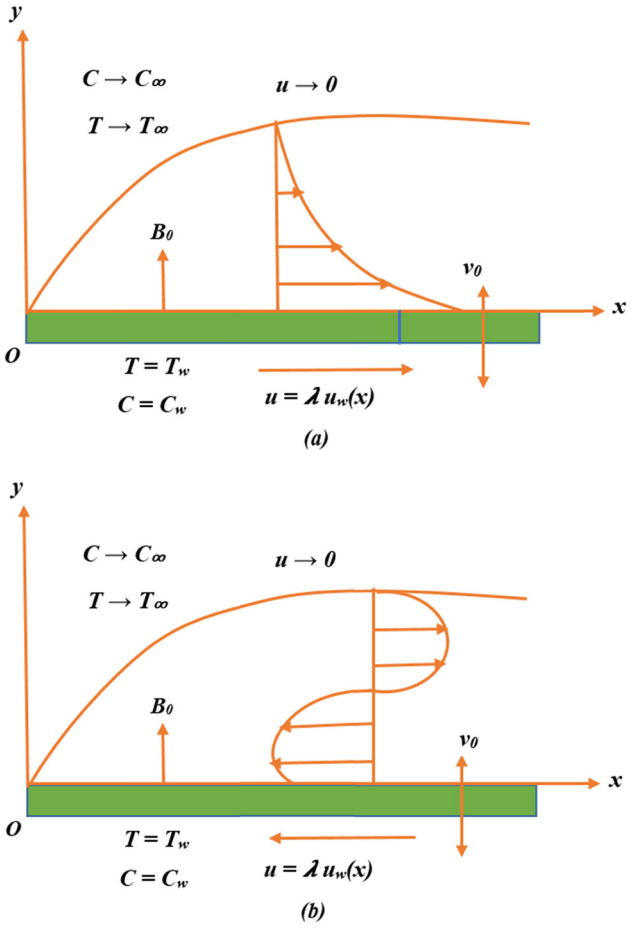

Figure 1: (a) Flow geometry for the stretching case. (b) Flow geometry for the shrinking case.

$$\begin{aligned} u\frac{\partial T}{\partial x} + v\frac{\partial T}{\partial y} &= \frac{k_{\text{hnf}}}{(\rho C_{\text{p}})_{\text{hnf}}}\frac{\partial^2 T}{\partial y^2} + \left(\frac{\sigma_{\text{hnf}}}{\rho_{\text{hnf}}}\right)B_0^2 u^2 + \left(\frac{\mu_{\text{hnf}}}{(\rho C_{\text{p}})_{\text{hnf}}}\right)\left(\frac{\partial u}{\partial z}\right)^2 \\ &\quad - \frac{1}{(\rho C_{\text{p}})_{\text{hnf}}}\frac{\partial q_{\text{r}}}{\partial y} - \lambda_1\left(u\frac{\partial u}{\partial x}\frac{\partial T}{\partial x} + v\frac{\partial u}{\partial y}\frac{\partial T}{\partial x} + u\frac{\partial T}{\partial y}\frac{\partial v}{\partial x}\right. \\ &\quad \left. + v\frac{\partial T}{\partial y}\frac{\partial v}{\partial y} + 2uv\frac{\partial^2 T}{\partial x \partial y} + u^2\frac{\partial^2 T}{\partial x^2} + v^2\frac{\partial T}{\partial y^2}\right), \end{aligned} \tag{3}$$

$$\begin{aligned} u\frac{\partial C}{\partial x} + v\frac{\partial C}{\partial y} &= D_{\text{B}}\frac{\partial^2 C}{\partial y^2} - K_{\text{r}}^2(C - C_\infty) \\ &\quad - \lambda_2\left(u\frac{\partial C}{\partial x}\frac{\partial u}{\partial x} + u\frac{\partial v}{\partial x}\frac{\partial C}{\partial y} + v\frac{\partial v}{\partial y}\frac{\partial C}{\partial y}\right. \\ &\quad \left. + v\frac{\partial C}{\partial x}\frac{\partial u}{\partial y} + 2uv\frac{\partial^2 C}{\partial x \partial y} + u^2\frac{\partial^2 C}{\partial x^2}\right. \\ &\quad \left. + v^2\frac{\partial C}{\partial y^2}\right). \end{aligned} \tag{4}$$

The radiative heat flux q_r is described as follows:

$$q_{\mathrm{r}} = -\frac{4\sigma^*}{3k^*}\frac{\partial T^4}{\partial y}, \quad T^4 \cong 4T_\infty^3 T - 3T_\infty^4. \tag{5}$$

The associated constraints at the boundary are defined as follows:

$$\begin{aligned} &u = \lambda a x + \varphi_0 \frac{\partial u}{\partial y}, \quad v = v_0, \quad T = T_{\mathrm{w}} + A\frac{\partial T}{\partial y}, \\ &C = C_{\mathrm{w}} + B\frac{\partial C}{\partial y} \ \text{ at } \ y = 0 \\ &u \to 0, \quad C \to C_\infty, \quad T \to T_\infty \ \text{ as } \ y \to \infty. \end{aligned} \tag{6}$$

Table 1 demonstrates the thermo-physical relations for mono and hybrid nanofluids.

Table 2 shows the numerical values of thermophysical properties of H_2O, Al_2O_3, and Cu.

Here, φ_1 and φ_2 show the Cu and Al_2O_3 nanoparticles' volume fractions, respectively, $n1$ shows Cu nanoparticles, and $n2$ shows Al_2O_3 nanoparticles. The symbol ρ shows the density, μ the dynamic viscosity, C_{p} the specific heat capacity, σ the electrical conductivity, and k the thermal conductivity of the fluid. The subscript f represents the fluid, nf the nanofluid, and hnf the hybrid nanofluid.

The similarity variables are defined as follows:

$$\begin{aligned} &\psi = \sqrt{av_{\mathrm{f}}}\, x f(\xi), \quad u = \frac{\partial \psi}{\partial y} = axf'(\xi), \\ &v = -\frac{\partial \psi}{\partial x} = -\sqrt{av_{\mathrm{f}}}\, f(\xi), \quad \phi(\xi) = \frac{C - C_\infty}{C_{\mathrm{w}} - C_\infty}, \\ &\theta(\xi) = \frac{T - T_\infty}{T_{\mathrm{w}} - T_\infty}, \quad \xi = y\sqrt{\frac{a}{v_{\mathrm{f}}}}. \end{aligned} \tag{7}$$

The terms ψ and v_{f} show the stream function and kinematic viscosity, respectively.

Substituting Eq. (8) in Eqs. (1)–(4), we have

Table 2: Thermophysical properties in the numerical form for H_2O, Al_2O_3, and Cu [51–53]

Physical properties	ρ (kg/m^3)	C_{p} (JK/g K)	σ (W/m K)	k (W/m K)
H_2O	997.1	4,179	5.5×10^{-6}	0.613
Al_2O_3	3,970	765	1×10^{-7}	40
Cu	8,933	385	5.96×10^{6}	401

$$\left(\frac{\mu_{\mathrm{hmf}}/\mu_{\mathrm{f}}}{\rho_{\mathrm{hnf}}/\rho_{\mathrm{f}}}\right)f''' + ff'' - f'^2 - \left(\frac{\sigma_{\mathrm{hnf}}/\sigma_{\mathrm{f}}}{\rho_{\mathrm{hnf}}/\rho_{\mathrm{f}}}\right)Mf' = 0, \tag{8}$$

$$\begin{aligned} &\frac{(\rho C_{\mathrm{p}})_{\mathrm{f}}}{(\rho C_{\mathrm{p}})_{\mathrm{hnf}}}\left(\frac{k_{\mathrm{hnf}}}{k_{\mathrm{f}}} + \mathrm{Rd}\right)\theta'' + \mathrm{Pr}f\theta' \\ &\quad + \frac{\sigma_{\mathrm{hmf}}/\sigma_f}{(\rho C_{\mathrm{p}})_{\mathrm{hnf}}/(\rho C_{\mathrm{p}})_{\mathrm{f}}}\mathrm{PrMEc}f'^2 \\ &\quad + \frac{\mu_{\mathrm{hnf}}/\mu_{\mathrm{f}}}{(\rho C_{\mathrm{p}})_{\mathrm{hnf}}/(\rho C_{\mathrm{p}})_{\mathrm{f}}}\mathrm{PrEc}Mf''^2 \\ &\quad - \delta\mathrm{Pr}(ff'\theta' + f^2\theta'') = 0, \end{aligned} \tag{9}$$

$$\phi'' + \mathrm{Sc}f\phi' - \beta\mathrm{Sc}(ff'\phi' + f^2\phi'') - \mathrm{KrSc}\phi = 0. \tag{10}$$

The associated boundary constraints are

$$\begin{aligned} &f(0) = s, \quad f'(0) = \lambda + \alpha f''(0), \quad \theta(0) = 1 + \gamma\theta'(0), \\ &\phi(0) = 1 + \chi\phi'(0), \\ &f' \to 0, \quad \phi \to 0, \quad \theta \to 0, \quad \text{as } \ \xi \to 0. \end{aligned} \tag{11}$$

The embedded factors are defined as

$$\left\{\begin{aligned} &s = -\frac{v_0}{\sqrt{av_{\mathrm{f}}}}, \quad \delta = \lambda_1 a, \quad M = \frac{\sigma_{\mathrm{f}}B_0^2}{\rho_{\mathrm{f}}a}, \quad \mathrm{Rd} = \frac{16\sigma^* T_\infty^3}{3k^* k_{\mathrm{f}}}, \\ &\mathrm{Pr} = \frac{(\mu C_{\mathrm{p}})_f}{k_{\mathrm{f}}}, \quad \mathrm{Kr} = \frac{K_{\mathrm{r}}^2}{a}, \mathrm{Ec} = \frac{u_{\mathrm{w}}^2(x)}{(C_{\mathrm{p}})_{\mathrm{f}}(T_{\mathrm{w}} - T_\infty)}, \quad \gamma = A\sqrt{\frac{a}{v_{\mathrm{f}}}}, \\ &\alpha = \varphi_0\sqrt{\frac{a}{v_{\mathrm{f}}}}, \quad \chi = B\sqrt{\frac{a}{v_{\mathrm{f}}}}, \quad \beta = \lambda_2 a, \quad \mathrm{Sc} = \frac{v_{\mathrm{f}}}{D_{\mathrm{B}}}. \end{aligned}\right\}$$

Table 1: Thermo-physical relations for mono and hybrid nanofluids

Properties	Nanofluid	Hybrid nanofluid
Dynamic viscosity	$\mu_{\mathrm{nf}} = \frac{\mu_{\mathrm{f}}}{(1-\varphi_1)^{2.5}}$	$\mu_{\mathrm{hnf}} = \frac{\mu_{\mathrm{f}}}{(1-\varphi_1-\varphi_2)^{2.5}}$
Heat capacity	$(\rho C_{\mathrm{p}})_{\mathrm{nf}} = (1-\varphi_1)(\rho C_{\mathrm{p}})_{\mathrm{f}} + \varphi_1(\rho C_{\mathrm{p}})_{n1}$	$(\rho C_{\mathrm{p}})_{\mathrm{hnf}} = \varphi_2(\rho C_{\mathrm{p}})_{n2} + (1-\varphi_2)[(1-\varphi_1)(\rho C_{\mathrm{p}})_{\mathrm{f}} + \varphi_1(\rho C_{\mathrm{p}})_{n1}]$
Density	$\rho_{\mathrm{nf}} = (1-\varphi_1)\rho_{\mathrm{f}} + \varphi_2\rho_{n1}$	$\rho_{\mathrm{hnf}} = (1-\varphi_2)[\rho_{\mathrm{f}}(1-\varphi_1) + \varphi_1\rho_{n_1}] + \varphi_2\rho_{n_2}$
Electrical conductivity	$\frac{\sigma_{\mathrm{nf}}}{\sigma_{\mathrm{f}}} = 1 + \frac{3\left(\frac{\sigma_{n1}}{\sigma_{\mathrm{f}}} - 1\right)\varphi_1}{\frac{\sigma_{n1}}{\sigma_{\mathrm{f}}} + 2 - \left(\frac{\sigma_{n1}}{\sigma_{\mathrm{f}}} - 1\right)\varphi_1}$,	$\frac{\sigma_{\mathrm{hnf}}}{\sigma_{\mathrm{nf}}} = 1 + \frac{3\left(\frac{\sigma_{n2}}{\sigma_{\mathrm{nf}}} - 1\right)\varphi_2}{\frac{\sigma_{n2}}{\sigma_{\mathrm{nf}}} + 2 - \left(\frac{\sigma_{n2}}{\sigma_{\mathrm{nf}}} - 1\right)\varphi_2}$
Thermal conductivity	$\frac{k_{\mathrm{nf}}}{k_{\mathrm{f}}} = \frac{k_{n1} + 2k_{\mathrm{f}} - 2\varphi_1(k_{\mathrm{f}} - k_{n1})}{k_{n1} + 2k_{\mathrm{f}} + \varphi_1(k_{\mathrm{f}} - k_{n1})}$	$\frac{k_{\mathrm{hnf}}}{k_{\mathrm{nf}}} = \frac{k_{n2} + 2k_{\mathrm{nf}} - 2\varphi_2(k_{\mathrm{nf}} - k_{n2})}{k_{n2} + 2k_{\mathrm{nf}} + \varphi_2(k_{\mathrm{nf}} - k_{n2})}$

2.1 Quantities of interest

The skin friction, Nusselt number, and Sherwood number are defined as

$$C_{fx} = \frac{\tau_{wx}}{\rho_f u_w^2}, \quad \mathrm{Nu}_x = \frac{x q_w}{k_f(T_w - T_\infty)}, \quad \mathrm{Sh}_x = \frac{x q_m}{D_B(C_w - C_\infty)}, \tag{12}$$

where

$$\tau_{wx} = \mu_{hnf}\frac{\partial u}{\partial z}\bigg|_{z=0}, \quad q_w = -k_{hnf}\frac{\partial T}{\partial z}\bigg|_{z=0} + q_r, \quad q_m = -D_B\frac{\partial C}{\partial z}\bigg|_{z=0}, \tag{13}$$

$$\sqrt{\mathrm{Re}_x}\,C_{fx} = \frac{\mu_{hnf}}{\mu_f}f''(0), \quad \frac{Nu_x}{\sqrt{\mathrm{Re}_x}} = -\left(\frac{k_{hnf}}{k_f} + \mathrm{Rd}\right)\theta'(0), \quad \frac{\mathrm{Sh}_x}{\sqrt{\mathrm{Re}_x}} = -\phi'(0). \tag{14}$$

Here, $\mathrm{Re}_x = \frac{ax^2}{\nu_f}$ represents the local Reynolds number.

3 Solution method

The bvp4c approach is applied for the solution of problem by incorporating the associated boundary conditions. The algorithm of this approach is based on the shooting technique. This technique needs to reduce the higher-order ODEs to the first-order ODEs with associated boundary conditions. This approach has many advantages and some disadvantages over other methods. Some of them are discussed as follows:

I. This approach consists of mesh points for discretization which is free from error and not time consuming.
II. This approach has the ability to handle multiple dependent variables, making it adaptable for solving complex coupled problems.
III. This approach employs an adaptive algorithm to refine mesh points where necessary, particularly in areas with rapid changes in the solution or boundary layers. This helps achieve accurate results with fewer mesh points.

This method has some disadvantages, which are discussed as follows:

I. This approach is primarily designed for solving up to fourth-order ordinary differential equations (ODEs), not ideal for higher-order or more complex systems.
II. The accuracy of the solution depends on how well the mesh is constructed; improper meshing can reduce the accuracy.
III. This approach is designed for ODEs and is not applicable to partial differential equations (PDEs) without transformation.

The following steps are taken while applying the bvp4c method:

I. Define the boundary value problem.
II. Define the similarity transformations.
III. Transform the PDEs to ODEs with associated boundary constraints.
IV. Write the boundary value problems as a first-order differential equations, so that the bvp4c scheme is easily applied.
V. Finally compute the required results numerically and graphically.

To get the computational solution of the problem, the following assumptions are applied:

$$\left.\begin{aligned} &f = y(1),\ f' = y(2),\ f'' = y(3),\ f''' = y'(3),\\ &\theta = y(4),\\ &\theta' = y(5),\ \theta'' = y'(5),\ \phi = y(6),\ \phi' = y(7),\\ &\phi'' = y'(7). \end{aligned}\right\} \tag{15}$$

Using Eq. (15), the above linear system of ODEs can be written as

$$y'(3) = \left\{\frac{A_2}{A_1}y(2)^2 - \frac{A_2}{A_1}y(1)y(3) + \frac{A_4}{A_1}My(2)\right\},$$

$$y'(5) = \left\{\begin{aligned} &\frac{A_5}{A_3 + \mathrm{Rd} - \delta y(1)^2}\mathrm{Pr}\ y(1)y(5)\\ &-\frac{A_4}{A_3 + \mathrm{Rd} - \delta y(1)^2}\mathrm{Pr}\ \mathrm{ME}\ cy(2)^2\\ &-\frac{A_1}{A_3 + \mathrm{Rd} - \delta y(1)^2}\mathrm{Pr}\ \mathrm{Ec}\ Qy(3)^2\\ &+\frac{A_5}{A_3 + \mathrm{Rd} - \delta y(1)^2}\delta\ \mathrm{Pr}\ y(1)y(2)y(5) \end{aligned}\right\}, \tag{16}$$

$$y'(7) = \left\{\begin{aligned} &-\frac{1}{1 + \beta\ \mathrm{Sc}\ y(1)^2}Scy(1)y(7)\\ &+\frac{1}{1 + \beta\ \mathrm{Sc}\ y(1)^2}\beta\ \mathrm{Sc}\ y(1)y(2)y(7)\\ &+\frac{1}{1 + \beta\ \mathrm{Sc}\ y(1)^2}\mathrm{Kr}\ \mathrm{Sc}\ y(6) \end{aligned}\right\}.$$

The transformed boundary conditions are as follows:

$$\left.\begin{aligned} &y_a(1) = s,\ y_a(2) = \lambda + \alpha y_a(3),\ y_b(2) - 0,\\ &y_a(4) = 1 + \gamma y_a(5),\ y_b(4) - 0,\\ &y_a(6) = 1 + \beta y_a(7),\ y_b(6) - 0. \end{aligned}\right\} \tag{17}$$

In the above equation, the subscripts a and b represent the corresponding constraints at $\xi = 0$ and $\xi \to \infty$, respectively.

Discretization is the process in which a differential equation can be approximated by using discrete values.

These equations can be solved by using numerical methods. In this method, the domain of the independent variable is divided into a grid of discrete points, and numerical schemes are used to approximate derivatives at these points. The shooting method is an iterative approach that transforms a boundary value problem into an initial value problem and then adjusts the initial guess to satisfy the boundary conditions. This method contained some steps, which are defined as follows:

- In this method, the initial guess for unknown is estimated at one boundary such as the starting point.
- This procedure is repeated each time modifying the initial condition guess and solving the IVP until the boundary condition is satisfied at the other points for the suggested accuracy.

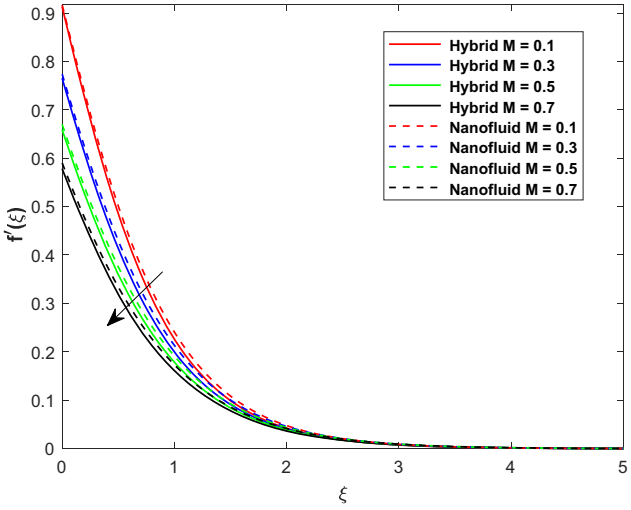

Figure 2: Effect of M on $f'(\xi)$.

4 Code validation

Table 3 is constructed to compare the results of skin friction for variations in stretching ratio parameter by keeping Ec = 0, Rd = 0.5, M = 0.5, Sc = 0, φ_1 = 0, and Kr = 0 with already-published results. The accuracy and validity of our model have been thoroughly verified by comparing our results with previously published data. This comparison, presented in Table 3, demonstrates a strong agreement between our findings and those reported in the literature, thereby confirming the correctness and reliability of the proposed model.

5 Discussion of graphical results

This portion discusses the impacts of diverse physical parameters on various flow profiles, as shown in Figures 2–14. The selected ranges for various factors provide stable and convergent solutions, ensuring the reliability of the result. These ranges are described as $(0.1 \le M \le .8)$, $(0.1 \le \gamma \le 0.7)$, $(0.1 \le s \le 0.5)$, $(1 \le \delta \le 4)$, $(1 \le \mathrm{Rd} \le 4)$, $(0.1 \le \alpha \le 0.4)$, $(0.1 \le \mathrm{Ec} \le 0.7)$, $(0.1 \le \mathrm{Sc} \le 0.7)$, $(0.2 \le \mathrm{Kr} \le 0.8)$, $(0.2 \le \beta \le 0.8)$, and $(0.1 \le \chi \le 0.8)$. The only restriction that bounds us is to fix the Prandtl number (Pr) at 6.2 (for water as the base fluid). Figures 2 and 3 describe impacts of M on $f'(\xi)$ and $\theta(\xi)$. Here, it is revealed that the velocity plot decreases with large values of M; however, an opposite tendency is witnessed in the temperature plot. The reason due to which the velocity profiles decrease with variations in M is the Lorentz force created by a strong magnetic force. This force behaves as a resistive force perpendicular to the direction of the flow field, opposing the fluid's motion. Hence, retardation is perceived in velocity profiles. Additionally, the higher M

Table 3: Comparison of current results for skin friction for variations in λ

	$f''(0)$		
λ	Bachok *et al.* [54]	Waini *et al.* [55]	Current outcomes
2	−1.88730	−1.887307	−1.88190
1	0	0	0
0.5	0.713295	0.71329	0.71369
0	1.23258	1.23258	1.2360
−0.5	1.495670	1.49567	1.49369
−1	1.328817	1.32881	1.33620

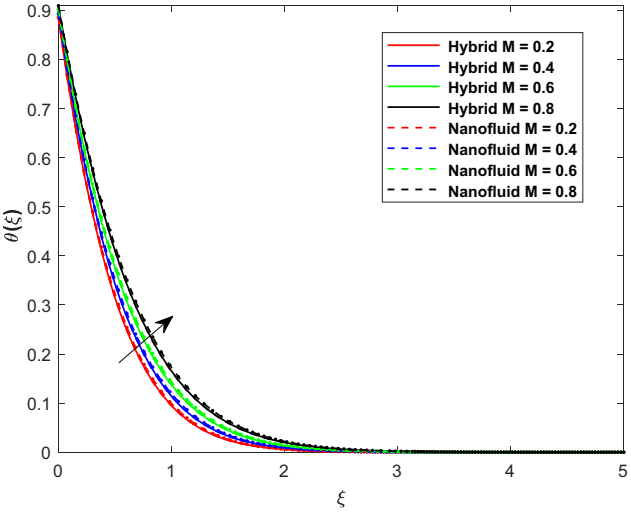

Figure 3: Effect of M on $\theta(\xi)$.

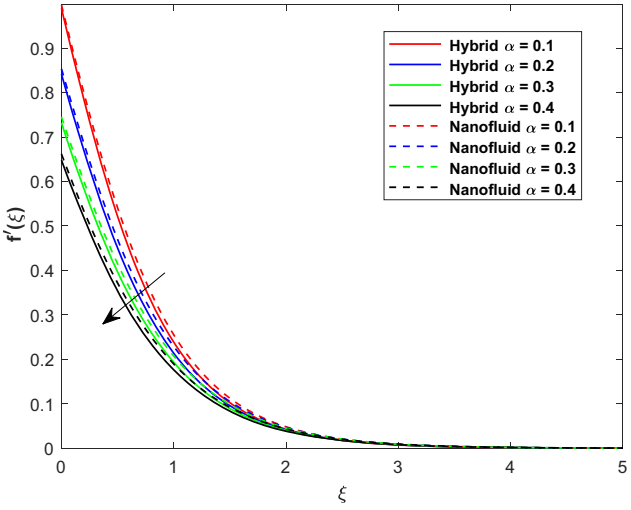

Figure 4: Effect of α on $f'(\xi)$.

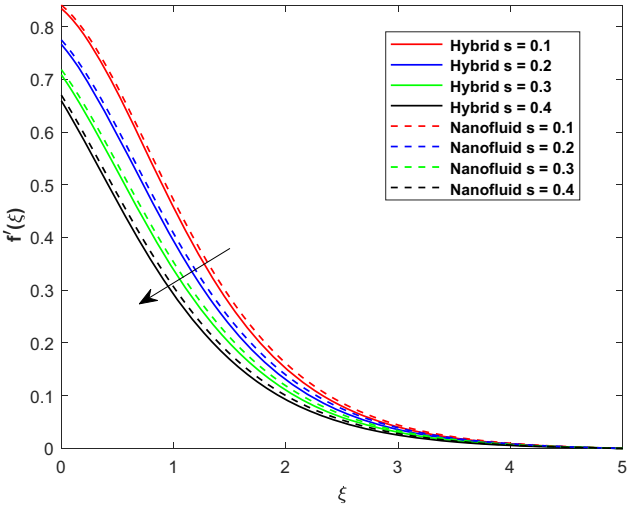

Figure 6: Effect of s on $f'(\xi)$.

reduces the thermal boundary of fluid particles, which increases the temperature plot. Figure 4 demonstrates the performance of a slip factor on $f'(\xi)$. The profile $f'(\xi)$ decreases with an increase in α. A higher slip factor leads to reduced diffusion of the fixed surface along the boundary layer, resulting in a thinner layer at the boundary. Additionally, as the slip factor increases, the flow slows down, which causes the skin friction to reduce. The impact of γ on $\theta(\xi)$ is displayed in Figure 5. A declining behavior is witnessed in $\theta(\xi)$ *via* the thermal slip factor. The reason for this is that when slip grows, the temperature gradient between solid and adjacent fluid layers in the boundary region increases. This leads to an increase in the heat transfer from the fluid to surface, which lowers the temperature in a thermal boundary layer. Figures 6 and 7 represent the influence of s on $f'(0)$ and $\theta(\xi)$. Temperature and velocity plots reduce with higher values of s. This is because a larger estimate of s causes a decline in the momentum and thickness of the thermal layer at the edge, which leads to the lessening of the velocity and temperature. Figure 8 shows the impression of δ on $\theta(\xi)$. In this figure, a lessening behavior is noted in $\theta(\xi)$ for growth in δ. Physically, for greater values of δ, the fluid particles require extra heat to transfer to their adjusting particles, which causes a lessening of the fluid temperature. The impact of Rd on $\theta(\xi)$ is shown in Figure 9. Here, an improvement in $\theta(\xi)$ is revealed. Radiation is a process of transferring heat which needs energy through fluid particles. Therefore, it creates heat energy in the fluid flow, which as a result increases the thickness of the boundary

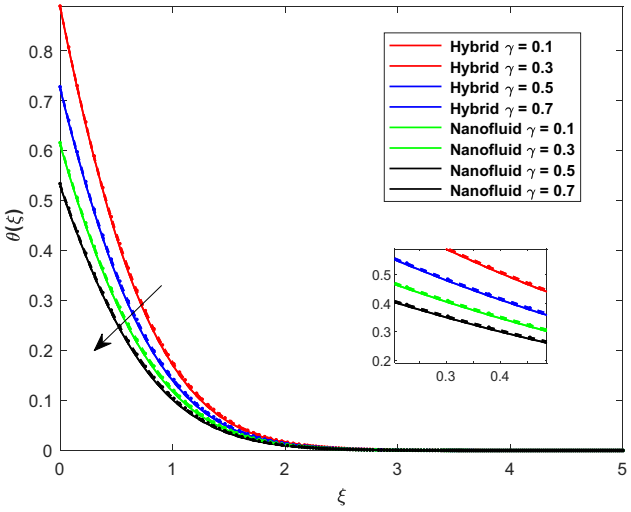

Figure 5: Effect of γ on $\theta(\xi)$.

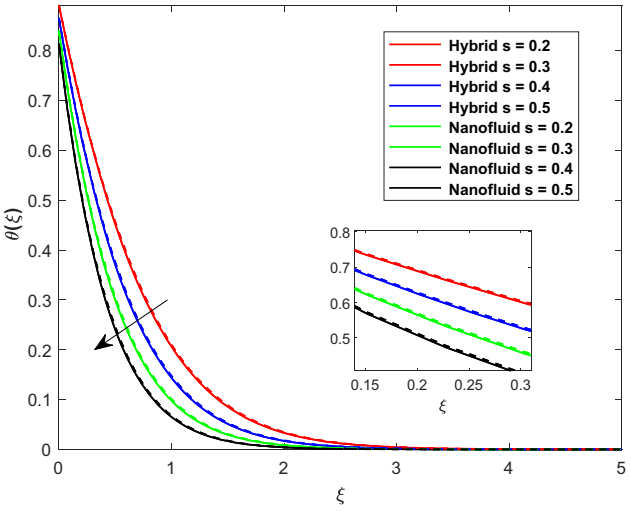

Figure 7: Effect of s on $\theta(\xi)$.

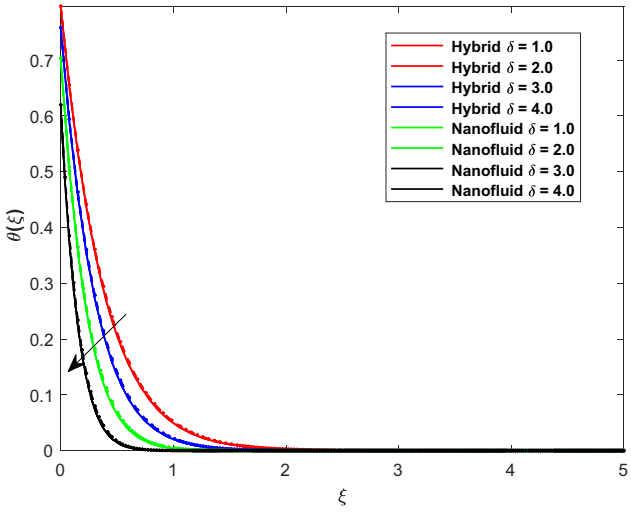

Figure 8: Effect of δ on $\theta(\xi)$.

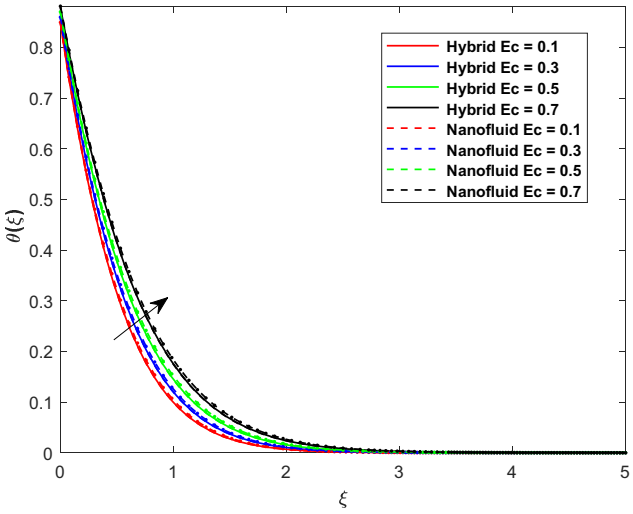

Figure 10: Effect of Ec on $\theta(\xi)$.

layer and the temperature of the fluid. Figure 10 specifies the outcome of Ec on the temperature plot. The higher Ec heightens the temperature plot, as noticed in this figure. An increase in Ec augments the dynamic energy of nanoparticles and increases the temperature at the edge. As a result, $\theta(\xi)$ escalates. Moreover, thermal conductivity of water is higher, so the temperature of the water-based hybrid nanofluid is superior. The effect on $\phi(\xi)$ through Kr is described in Figure 11. It is perceived in this figure that the augmented values of Kr decline $\phi(\xi)$. Actually, higher chemical reaction thickens the width of the concentration layer at the boundary, which ultimately declines the concentration at the surface of the sheet. Hence, a decreasing behavior is perceived in $\phi(\xi)$. Figure 12 is considered to present the effect of the solutal relaxation time parameter β on $\phi(\xi)$. It is perceived here that the concentration and thickness at the boundary decrease with growth in β. Nanoparticles require additional time to diffuse into the neighboring area, which causes an increase in the concentration relaxation time. Hence, thickness of the concentration layer at the boundary declines, causing a reduction in concentration profiles. The sketch in Figure 13 shows the impact of Sc on $\phi(\xi)$. It is observed in this figure that $\phi(\xi)$ diminishes with higher Sc. Physically, an increase in Sc decreases the mass diffusivity, which causes the decline in $\phi(\xi)$. Figure 14 is constructed to show the influence of χ on $\phi(\xi)$. The $\phi(\xi)$ profiles reduce with higher χ. It is due to this reason that the slip factor decreases the motion of fluid, which presents a decrease in the net molecular movement, and thus the concentration profile falls

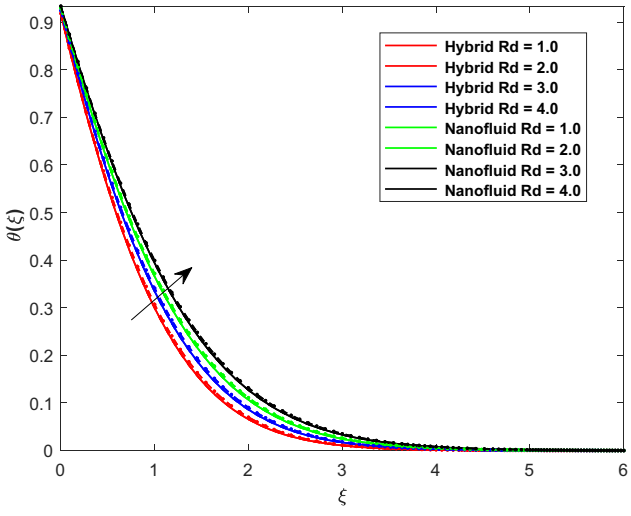

Figure 9: Effect of Rd on in $\theta(\xi)$.

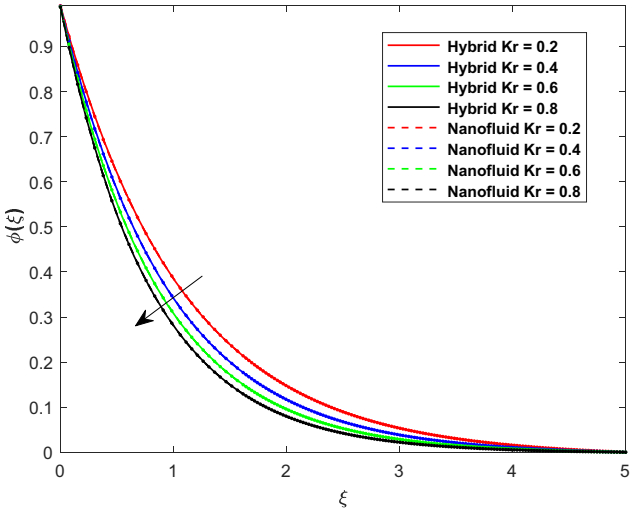

Figure 11: Effect of Kr on $\phi(\xi)$.

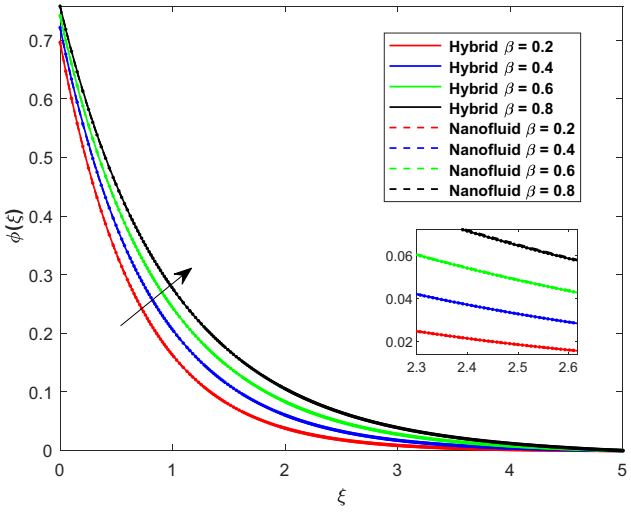

Figure 12: Effect of β on $\phi(\xi)$.

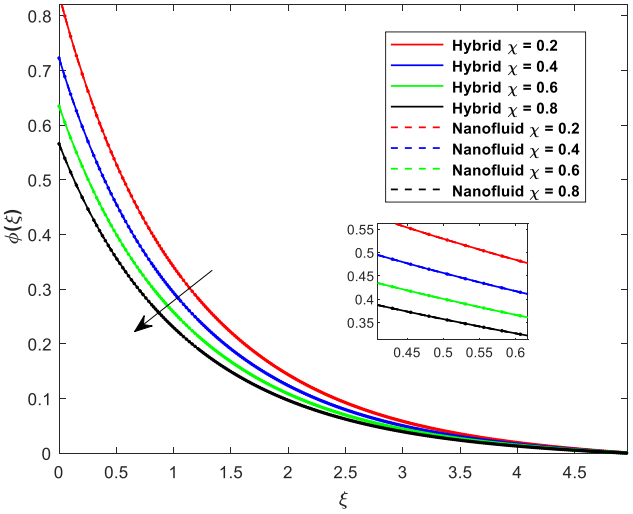

Figure 14: Effect of χ on $\phi(\xi)$.

with less molecular movement. The influence of various parameters on $\sqrt{\mathrm{Re}_x}C_{fx}$, $\frac{\mathrm{Nu}_x}{\sqrt{\mathrm{Re}_x}}$ and $\frac{\mathrm{Sh}_x}{\sqrt{\mathrm{Re}_x}}$ is demonstrated in Tables 4–6. From Table 4, the numerical data revealed that the surface drag force upsurges with growth in M, λ, and s; however, it decreases with escalation in α. Augmentations in M produce a Lorentz force which disturbs the motion of fluid. This opposing force increases the friction at the surface as a result of which the drag force increases. Table 5 fluctuates the impression of Rd, Ec, δ and γ on Nusselt number. It is perceived from this table that the Nusselt number augments with an increment in these parameters. The greater Ec changes the kinetic energy into thermal energy. This causes an increase in the thermal characteristic of fluids, and as a result the heat transformation rate increases. However, an opposite trend is noticed for growth in M in the behavior of Nusselt number. Table 6 portrays the impact of Sc, β, χ, and Kr on $\frac{\mathrm{Sh}_x}{\sqrt{\mathrm{Re}_x}}$. The mass transfer rate of hybrid nanofluid shows a declining behavior through growth in these parameters. Figure 15 highlights the streamlines for $f'(\xi)$ *via* M.

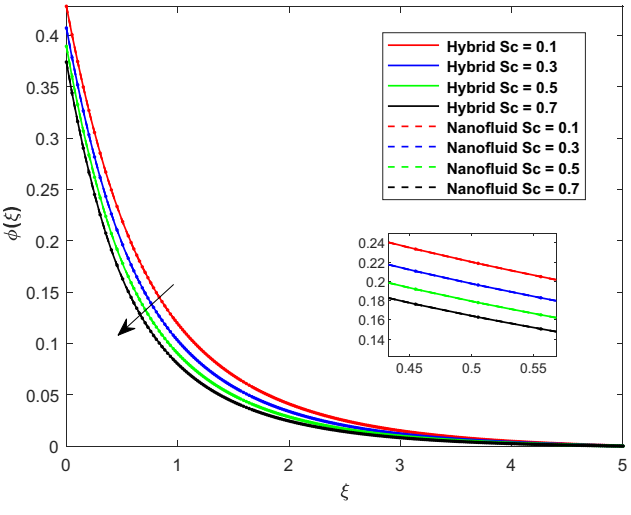

Figure 13: Effect of Sc on $\phi(\xi)$.

6 Final remarks

In this study, the Cattaneo–Christov heat and mass flux phenomenon is considered to examine the electrically conducting flow of hybrid nanofluids across a stretching/shrinking sheet with slip and suction/injection effects. The nanoparticles of copper and alumina are homogeneously dispersed in water as the host fluid. Incorporating the thermal radiation effects in the energy equation suggests a strong heat

Table 4: Effect of different factors on $\sqrt{\mathrm{Re}_x}C_{fx}$ of hybrid nanofluids

M	λ	α	s	$\sqrt{\mathrm{Re}_x}C_{fx}$
0.5				0.5323
1				0.5324
1.5				0.5325
	0.1			0.0420
	0.2			0.1063
	0.3			0.1865
		1		0.5358
		2		0.3326
		3		0.2441
			1	0.6532
			2	0.7445
			3	0.8057

Table 5: Effect of different factors on $\frac{Nu_x}{\sqrt{Re_x}}$ of hybrid nanofluids

M	δ	γ	Rd	Ec	$\frac{Nu_x}{\sqrt{Re_x}}$
1					0.3221
2					0.3222
3					0.3223
	0.1				0.5965
	0.2				0.5688
	0.3				0.5489
		0.1			0.3965
		0.2			0.3724
		0.3			0.3285
			0.6		0.2215
			0.7		0.1993
			0.8		0.1805
				0.1	0.5004
				0.3	0.3285
				0.5	0.2629

source in the vicinity of a sheet's surface. The leading equations in a dimensionless form have been solved through the bvp4c approach. The incorporation of slip conditions and suction/injection effects enhances the understanding of realistic flow behavior, particularly in experimental engineering applications. The incorporation of thermal radiation highlights the influence of high heat flux phenomena, making the study more applicable in cooling systems and heat exchangers.

The major key points that are concluded from this investigation are given as follows:

1) The increasing magnetic parameter diminishes the velocity curve because of the higher Lorentz force.

Table 6: Effect of various parameters on $\frac{Sh_x}{\sqrt{Re_x}}$ of hybrid nanofluids

Sc	β	χ	Kr	$\frac{Sh_x}{\sqrt{Re_x}}$
0.6				0.3666
0.7				0.3436
0.8				0.3223
	0.1			0.9561
	0.2			0.8727
	0.3			0.8026
		0.1		0.8727
		0.2		0.8661
		0.3		0.8596
			0.1	0.2016
			0.2	0.1857
			0.3	0.1693
				−0.5004
				−0.3285
				−0.2629

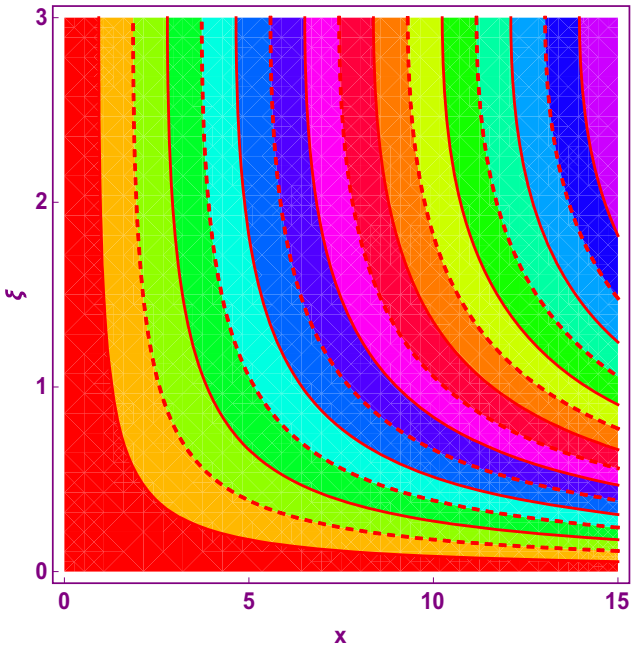

Figure 15: Streamlines *via M*.

2) The higher velocity slip parameter diminishes the velocity plot.
3) It is witnessed that the augmented estimation of the suction factor declines the velocity curve.
4) An upsurge in the thermal slip factor declines the temperature distribution.
5) The temperature curve increases with a surge in the Eckert number and magnetic and thermal radiation parameters.
6) Concentration distribution shows a declining behavior with higher Schmidt number, chemical reaction, and solutal relaxation time factors.
7) It is interesting to note that the surface drag force escalates with large values of magnetic parameter; however, it reduces with suction in the slip parameter.
8) The heat transfer rate shows an improvement, with an increase in thermal radiation and Eckert number; whereas it decreases with a surge in the thermal slip parameter and thermal relaxation time parameter.
9) Declining performance is perceived in the magnitude of mass transfer rate through surge in the chemical reaction, Schmidt number, and concentration slip parameter.

This study has some limitations such as it focuses on specified geometry, which may not generalize to complex geometries such as wedge, cone and curved sheets. This study contemplates the Cattaneo–Christov model which accounts for finite speed mass and thermal transport but

may not be applicable for higher speed of fluid flow and temperature gradients. This model focuses on two-dimensional steady flow, which limits the study to three-dimensional and transient flow behavior.

This work will play a vital role in industry and real-world engineering problems such as energy efficiency increase, manufacturing processes, renewable energy systems, thermal management, and micro channels.

Funding information: This study is supported *via* funding from Prince Sattam bin Abdulaziz University project number (PSAU/2025/R/1446).

Author contributions: Ebrahem A. Algehyne: conceptualization, methodology, software, writing – reviewing and editing. Fahad Maqbul Alamrani: data curation, writing – reviewing and editing. M.M. Seada: visualization, investigation. Anwar Saeed: software, validation, supervision. Gabriella Bognár: writing – original draft preparation. All authors have accepted responsibility for the entire content of this manuscript and approved its submission.

Conflict of interest: The authors state no conflict of interest.

Data availability statement: The datasets generated and/or analyzed during the current study are available from the corresponding author on reasonable request.

References

[1] Dey D, Makinde OD, Borah R. Analysis of dual solutions in MHD fluid flow with heat and mass transfer past an exponentially shrinking/stretching surface in a porous medium. Int J Appl Comput Math. 2022;8(2):66.

[2] Vishalakshi AB, Maranna T, Mahabaleshwar US, Laroze D. An effect of MHD on non-Newtonian fluid flow over a porous stretching/shrinking sheet with heat transfer. Appl Sci. 2022;12(10):4937.

[3] Abbas A, Jeelani MB, Alnahdi AS, Ilyas A. MHD Williamson nanofluid fluid flow and heat transfer past a non-linear stretching sheet implanted in a porous medium: effects of heat generation and viscous dissipation. Processes. 2022;10(6):1221.

[4] Bafakeeh OT, Raghunath K, Ali F, Khalid M, Tag-ElDin ESM, Oreijah M, et al. Hall current and Soret effects on unsteady MHD rotating flow of second-grade fluid through porous media under the influences of thermal radiation and chemical reactions. Catalysts. 2022;12(10):1233.

[5] Khan A, Gul T, Ali I, Khalifa HAE-W, Muhammad T, Alghamdi W, et al. Thermal examination for double diffusive MHD Jeffrey fluid flow through the space of disc and cone apparatus subject to impact of multiple rotations. Int J Heat Fluid Flow. 2024;106:109295.

[6] Mahabaleshwar US, Sneha KN, Chan A, Zeidan D. An effect of MHD fluid flow heat transfer using CNTs with thermal radiation and heat source/sink across a stretching/shrinking sheet. Int Commun Heat Mass Transf. 2022;135:106080.

[7] Obalalu AM, Alqarni MM, Odetunde C, Memon MA, Olayemi OA, Shobo AB, et al. Improving agricultural efficiency with solar-powered tractors and magnetohydrodynamic entropy generation in copper–silver nanofluid flow. Case Stud Therm Eng. 2023;51:103603.

[8] Acheson CR, Głowacki J, Parashar TN, Wimbush SC. Computational modelling of superconducting applied-field magnetoplasmadynamic thrusters: How does magnetic shielding influence thrust?. In Proc. 37th International Electric Propulsion Conference; 2022.

[9] Nadeem M, Siddique I, Bilal M, Anjum K. Numerical study of MHD Prandtl Eyring fuzzy hybrid nanofluid flow over a wedge. Numer Heat Transf Part A Appl. 2023;85(24):4328–44.

[10] Vanitha GP, Mahabaleshwar US, Hatami M, Yang X. Heat and mass transfer of micropolar liquid flow due to porous stretching/shrinking surface with ternary nanoparticles. Sci Rep. 2023;13(1):3011.

[11] Khan S, Selim MM, Khan A, Ullah A, Abdeljawad T, Ikramullah M, et al. On the analysis of the non-Newtonian fluid flow past a stretching/shrinking permeable surface with heat and mass transfer. Coatings. 2021;11(5):566.

[12] Sharma S, Dadheech A, Parmar A, Arora J, Al-Mdallal Q, Saranya S. MHD micro polar fluid flow over a stretching surface with melting and slip effect. Sci Rep. 2023;13(1):10715.

[13] Roşca NC, Roşca AV, Pop I. Dual solutions on three-dimensional nanofluid flow and heat transfer over a permeable non-linearly shrinking surface with second-order velocity slips. Int J Numer Methods Heat Fluid Flow. 2023;33(7):2392–408.

[14] Jamaludin A, Nasir NAAM, Nazar R, Pop I. MHD opposing flow of Cu – TiO_2 hybrid nanofluid under an exponentially stretching/shrinking surface embedded in porous media with heat source and slip impacts. Results Eng. 2023;17:101005.

[15] Boujelbene M, Rehman S, Jazaa Y, Dhaou MH. Thermodynamics of hydromagnetic boundary layer flow of Prandtl nanofluid past a heated stretching cylindrical surface with interface slip. J Taiwan Inst Chem Eng. 2024;155:105310.

[16] Algehyne EA, Alamrani FM, Khan A, Khan KA, Lone SA, Saeed A. On thermal distribution of MHD mixed convective flow of a Casson hybrid nanofluid over an exponentially stretching surface with impact of chemical reaction and ohmic heating. Colloid Polym Sci. 2023;302(4):1–14.

[17] Parvin S, Isa SSPM, Al-Duais FS, Hussain SM, Jamshed W, Safdar R, et al. The flow, thermal and mass properties of Soret-Dufour model of magnetized Maxwell nanofluid flow over a shrinkage inclined surface. PLoS One. 2022;17(4):e0267148. doi: 10.1371/JOURNAL.PONE.0267148.

[18] Sachhin SM, Mahabaleshwar US, Huang HN, Sunden B, Zeidan D. An influence of temperature jump and Navier's slip-on hybrid nano fluid flow over a permeable stretching/shrinking sheet with heat transfer and inclined MHD. Nanotechnology. 2023;35(11):115401.

[19] Kumar S, Shaikh AA, Lanjwani HB, Shah SF. MHD flow and heat transfer of micropolar nanofluid on a linearly stretching/shrinking porous surface. VFAST Trans Math. 2023;11(1):141–54.

[20] Khan U, Zaib A, Ishak A, Waini I, Pop I, Elattar S, et al. Stagnation point flow of a water-based graphene-oxide over a stretching/shrinking sheet under an induced magnetic field with homogeneous-heterogeneous chemical reaction. J Magn Magn Mater. 2023;565:170287.

[21] Mahmood Z, Khan U. Unsteady three-dimensional nodal stagnation point flow of polymer-based ternary-hybrid nanofluid past a stretching surface with suction and heat source. Sci Prog. 2023;106(1):00368504231152741.
[22] Ilango MS, Lakshminarayana P. Induced magnetic field and Soret–Dufour effects on viscous dissipative Casson fluid flow through porous medium over a stretching sheet. J Therm Anal Calorim. 2024;149(15):8713–27.
[23] Yasmin H. Numerical investigation of heat and mass transfer study on MHD rotatory hybrid nanofluid flow over a stretching sheet with gyrotactic microorganisms. Ain Shams Eng J. 2024;15(9):102918.
[24] Mehmood R, Ali I, Ijaz S, Rana S, Maraj EN. Radiative slip transport of magnetized gyrotactic micro-organisms submerged with nano fluid along a vertical stretching surface with suction/injection effects. Proc Inst Mech Eng Part N J Nanomater Nanoeng Nanosyst. 2023;23977914231176864.
[25] Ilango MS, Lakshminarayana P. Effects of double diffusion and induced magnetic field on convective flow of a Casson nanofluid over a stretching surface. Heliyon. 2024;10(10):e31040.
[26] Mahesh R, Mahabaleshwar US, Aly EH, Manca O. An impact of CNTs on an MHD Casson Marangoni boundary layer flow over a porous medium with suction/injection and thermal radiation. Int Commun Heat Mass Transf. 2023;141:106561.
[27] Song M, Sukumar M, Raju CSK, Varma SVK, Ijaz Khan M, Awwad FA, et al. Inspection of Couette and pressure-driven Poiseuille entropy-optimized dissipated flow in a suction/injection horizontal channel: Analytical solutions. Open Phys. 2023;21(1):20230109.
[28] Saidulu B, Reddy KS. Comprehensive analysis of radiation impact on the transfer of heat and mass micropolar MHD free convective fluid flow across a stretching permeability sheet with suction/injection. Heat Transf. 2023;52(4):3317–32.
[29] Nihaal KM, Mahabaleshwar US. Heat and mass transfer analysis of hybrid nanofluid flow over a rotating permeable cylinder: a modified Buongiorno model approach. Hybrid Adv. 2024;6:100243.
[30] MS I, Pallavarapu L. Melting heat transfer and entropy analysis of MHD Casson nanofluid flow through a stretchy surface with Joule heating and complete slip. World J Eng. 2024. doi: 10.1108/WJE-01-2024-0016.
[31] Gopi Krishna G, Ramanuja M, Mishra S, Ramanjini V, Sudhakar A, Kavitha J. Exploration of radiative heat on the Jeffery fluid flow in a microchannel for the impact of suction/injection. Heat Transf. 2023;52(2):1097–117.
[32] Reddy NN, Reddy YD, Rao VS, Goud BS, Nisar KS. Multiple slip effects on steady MHD flow past a non-isothermal stretching surface in presence of Soret, Dufour with suction/injection. Int Commun Heat Mass Transf. 2022;134:106024.
[33] Bachok N, Tajuddin SNN, Anuar NS, Rosali H. Numerical computation of stagnation point flow and heat transfer over a nonlinear stretching/shrinking sheet in hybrid nanofluid with suction/injection effects. J Adv Res Fluid Mech Therm Sci. 2023;107(1):80–6.
[34] Asibor RE, Osuidia CF, Asibor VO, Okoro FM. Electro-osmotic transient magneto hydrodynamics flow and heat transfer analysis in plane channel. Int J Res Innov Appl Sci. 2024;9(6):369–83.
[35] Aly EH, Mahabaleshwar US, Anusha T, Usafzai WK, Pop I. Wall jet flow and heat transfer of a hybrid nanofluid subject to suction/injection with thermal radiation. Therm Sci Eng Prog. 2022;32:101294.
[36] Asibor RE, Ogunniyi O, Okedoye M. Reactivity effect of on unsteady hydromagnetic convective flow of reactive viscous fluid with chemical reaction and suction/injection. Niger J Eng Sci Res. 2023;6(1):47–59.
[37] Fourier JBJ. Théorie analytique de la chaleur. Paris: Gauthier-Villars et fils; 1888. p. 1.
[38] Fick A. Uber diffusion. Phil Mag. 10:30–9; Repr. 1995 as Diffus. J. Membr. Sci 100.1855;10, 33–38.
[39] Mahariq I, Ghazwani HA, Shah MA. Enhancing heat and mass transfer in MHD tetra hybrid nanofluid on solar collector plate through fractal operator analysis. Results Eng. 2024;24:103163.
[40] Cattaneo C. Sulla conduzione del calore. Atti Sem Mat Fis Univ Modena. 1948;3:83–101.
[41] Christov CI. On frame indifferent formulation of the Maxwell–Cattaneo model of finite-speed heat conduction. Mech Res Commun. 2009;36(4):481–6.
[42] Farooq U, Waqas H, Makki R, Ali MR, Alhushaybari A, Muhammad T, et al. Computation of Cattaneo-Christov heat and mass flux model in Williamson nanofluid flow with bioconvection and thermal radiation through a vertical slender cylinder. Case Stud Therm Eng. 2023;42:102736.
[43] Gowda RJP, Kumar RN, Kumar R, Prasannakumara BC. Three-dimensional coupled flow and heat transfer in non-Newtonian magnetic nanofluid: An application of Cattaneo-Christov heat flux model. J Magn Magn Mater. 2023;567:170329.
[44] Jawad M, Nisar KS. Upper-convected flow of Maxwell fluid near stagnation point through porous surface using Cattaneo-Christov heat flux model. Case Stud Therm Eng. 2023;48:103155.
[45] Shahzad F, Jamshed W, Sajid T, Shamshuddin MD, Safdar R, Salawu SO, et al. Electromagnetic control and dynamics of generalized burgers' nanoliquid flow containing motile microorganisms with Cattaneo–Christov relations: Galerkin finite element mechanism. Appl Sci. 2022;12(17):8636.
[46] Reddy MV, Vajravelu K, Ajithkumar M, Sucharitha G, Lakshminarayana P. Numerical treatment of entropy generation in convective MHD Williamson nanofluid flow with Cattaneo–Christov heat flux and suction/injection. Int J Model Simul. 2024;1–18.
[47] Ullah R, Israr Ur Rehman M, Hamid A, Arooj S, Khan WA. Heat and mass transport aspect on magnetised Jeffery fluid flow over a stretching cylinder with the Cattaneo–Christov heat flux model. Mol Phys. 2024;122(11):e2288701.
[48] Vinodkumar Reddy M, Ajithkumar M, Bin Zafar SS, Faizan M, Ali F, Lakshminarayana P. Magnetohydrodynamic stagnation point flow of Williamson hybrid nanofluid via stretching sheet in a porous medium with heat source and chemical reaction. Proc Inst Mech Eng Part E J Process Mech Eng. 2024;09544089241239583.
[49] Waini I, Ishak A, Pop I. Hybrid nanofluid flow over a permeable non-isothermal shrinking surface. Mathematics. 2021;9(5):538.
[50] Shehzad SA, Hayat T, Alsaedi A, Meraj MA. Cattaneo-Christov heat and mass flux model for 3D hydrodynamic flow of chemically reactive Maxwell liquid. Appl Math Mech. 2017;38:1347–56.
[51] Oztop HF, Abu-Nada E. Numerical study of natural convection in partially heated rectangular enclosures filled with nanofluids. Int J Heat Fluid Flow. 2008;29(5):1326–36.
[52] Sheikholeslami M, Gorji-Bandpy M, Ganji DD. Numerical investigation of MHD effects on Al2O3–water nanofluid flow and heat transfer in a semi-annulus enclosure using LBM. Energy. 2013;60:501–10.
[53] Hayat T, Ahmed B, Abbasi FM, Alsaedi A. Hydromagnetic peristalsis of water based nanofluids with temperature dependent viscosity: a comparative study. J Mol Liq. 2017;234:324–9.
[54] Bachok N, Ishak A, Pop I. Stagnation-point flow over a stretching/shrinking sheet in a nanofluid. Nanoscale Res Lett. 2011;6(1):1–10.
[55] Waini I, Ishak A, Pop I. Hiemenz flow over a shrinking sheet in a hybrid nanofluid. Results Phys. 2020;19:103351.